The BIMA Survey of Nearby Galaxies (BIMA SONG): I. The Radial Distribution of CO Emission in Spiral Galaxies

Michael W. Regan[1,2,3] Michele D. Thornley[4,5], Tamara T. Helfer[6,7,8], Kartik Sheth[3,9], Tony Wong[8], Stuart N. Vogel[9], Leo Blitz[8], and Douglas C.-J. Bock[8]

ABSTRACT

We present the first results of the BIMA Survey of Nearby Galaxies (BIMA SONG), an imaging survey of the CO J=(1−0) emission in 44 nearby spiral galaxies at a typical resolution of 6″. BIMA SONG differs from previous high-resolution CO surveys in that: (1) CO brightness was not an explicit selection criterion; (2) a larger area (200″ diameter for most galaxies) of each galaxy was imaged; and (3) fully-sampled single-dish CO data (55″ resolution) were obtained for over half of the sample galaxies, so all of the CO flux is imaged in these galaxies. Here we present CO maps for a subsample of 15 BIMA SONG galaxies for which we have also obtained near-infrared or optical broad-band data. The CO maps display a remarkable variety of molecular gas morphologies, and, as expected, the CO surface brightness distributions show considerably more substructure than the stellar light distributions, even when averaged over kiloparsec scales. The radial distribution of stellar light in galactic disks is generally characterized as an exponential. It is, therefore, of interest to investigate whether the molecular gas, which is the star-forming medium, has a similar distribution. Though our low-resolution single-dish radial profiles of CO emission can be

[1]Space Telescope Science Institute, 3700 San Martin Drive, Baltimore, MD 21218, mregan@stsci.edu

[2]Carnegie Institution of Washington, Department of Terrestrial Magnetism

[3]Visting Astronomer, Kitt Peak National Observatory, National Optical Astronomy Observatories, which are operated by the Association of Universities for Research in Astronomy, Inc. (AURA) under cooperative agreement with the National Science Foundation

[4]National Radio Astronomy Observatory, Charlottesville, VA 22903

[5]Physics Department, Bucknell University, Lewisburg, PA 17837

[6]National Radio Astronomy Observatory, Tucson, AZ 85721

[7]Steward Observatory, University of Arizona, Tucson, AZ 85721

[8]Radio Astronomy Laboratory, University of California, Berkeley, CA 94720

[9]Department of Astronomy, University of Maryland, College Park, MD 20742

described by simple exponentials, this is not true for the emission at our full 6″ resolution. The scale lengths of the CO disks are correlated with the scale lengths of the stellar disks with a mean ratio of the scale lengths of about one. There is, however, considerable intrinsic scatter in the correlation. We also find that: (1) there is also a weak correlation between the ratio of K-band to CO luminosity and Hubble type; (2) in half of the galaxies presented here, CO emission does not peak at the location of the stellar nucleus; (3) averaged over the inner kiloparsec, the CO emission in one-half of the galaxies exhibits an excess over that expected from an exponential disk which is similar to the excess in stellar light caused by the bulge stars; and (4) this excess CO emission may be due to an increase in the total molecular gas content in the bulge region, or alternatively, to an increase in the CO emissivity caused by the increased pressure of the bulge region.

1. Introduction

The evolution of a spiral galaxy is intricately linked to its molecular gas through a variety of processes. All available evidence suggests that molecular gas fuels star formation both in the Milky Way (Blitz 1993, and references therein) and in other galaxies as can be seen through its importance to studies of triggered star formation in spiral arms (Vogel, Kulkarni & Scoville 1988), nuclear starbursts (Young & Devereux 1991; Aalto et al. 1995; Planesas, Colina & Perez-Olea 1997), and the increased star formation seen at bar ends (Regan et al. 1996; Sheth et al. 2000). In addition, molecular gas can affect galaxy evolution through inflow to the nuclear region (e.g. through bar or interaction driven inflow). This inflow may contribute to non-stellar activity in the nucleus, change the central mass concentration, cause a bar to be destroyed (Norman, Sellwood & Hasan 1996), or trigger a late Hubble type galaxy to evolve into an earlier type (e.g., Friedli & Martinet 1993).

The bulk of our knowledge about molecular gas in galaxies comes from studies of carbon monoxide (CO) emission, primarily in its lowest rotational transition (CO J=1−0, λ=2.6mm). CO is used as a tracer of H_2, which lacks a permanent dipole moment and is therefore undetectable at the temperatures of typical molecular clouds (see review of CO observations in galaxies by Young & Scoville 1991). Observations of CO have been made in several hundred external galaxies (for data prior to 1990 see catalogs in Verter 1985, 1990), with the largest uniform study being the FCRAO Extragalactic CO Survey (Young et al. 1995), which presented spectra from 1412 positions in 300 galaxies. Such observations have served as the basis for our statistical understanding of the molecular content of galaxies as a function of parameters like Hubble type and luminosity.

However, the distribution and physical conditions of molecular gas on small scales within galaxies are still poorly understood. The overwhelming majority of extragalactic observations have been carried out using single-dish telescopes, with linear resolutions which are typically many kiloparsecs. Observations at this resolution resolve structures which are about one hundred times larger in diameter than a giant molecular cloud (GMC), the basic unit into which molecular gas is organized in the Milky Way. Outside of the Local Group to achieve the sub-kiloparsec resolution needed to study the distribution of molecular gas in galaxies, it is necessary to use an interferometer for all but the nearest galaxies. So far, the largest interferometric study of external galaxies has been the recent survey presented by Sakamoto et al. (1999a), which mapped the central CO distribution in 20 nearby spiral galaxies with the Nobeyama Radio Observatory (NRO) and the Owens Valley Radio Observatory (OVRO) millimeter interferometers. The Sakamoto et al. (1999a) survey achieved $4''$ resolution over the central region, within $30''$ of the center, and focused on how the distribution of molecular gas in the central kiloparsec differs in galaxies with and without strong nuclear activity (Sakamoto et al. 1999b).

The limited field of view and possible "missing flux" of the Sakamoto et al. (1999a) and other interferometer-only surveys (Jogee 1999; Regan, Sheth & Vogel 1999) prevent us from making a quantitative comparison of the molecular and stellar distributions in the galaxies studied. Meanwhile, the resolution of the single dish surveys is not high enough to investigate the connection between features in the stellar distribution (bars, spiral arms, and bulges) and the molecular distribution. To accurately investigate the sub-kiloparsec-scale molecular gas distributions in galaxies, we have undertaken the BIMA Survey of Nearby Galaxies (BIMA SONG), a systematic imaging survey of CO emission in the centers and inner disks of an objectively selected sample of 44 nearby spiral galaxies. The database we are producing from the survey includes spatial-velocity data cubes showing the distribution and kinematics of CO emission at resolutions of a few hundred parsecs ($\sim 6''$) and ~ 10 km s^{-1} over a field of view of typically 10 kiloparsecs ($\sim 190''$). The BIMA SONG maps for over half of the 44 sample galaxies incorporate single dish data taken with the NRAO 12m telescope; these maps, therefore, do not suffer from the "missing flux" problem to which interferometric images are often susceptible. For the remaining galaxies, we collected sensitive spectra from the NRAO 12m telescope so that we could assess how much, if any, of the single dish flux is missing in the BIMA-only maps. BIMA SONG differs from previous high-resolution CO surveys in the following ways: (1) CO brightness was not an explicit selection criterion, as we observed all nearby, optically-bright spirals with suitable declinations and inclinations (except M33); (2) we observed a much larger area of each galaxy, covering a significant fraction of the optical disk; (3) we observed all sample galaxies using uniform criteria, and reduced and analyzed all the data using well-defined, uniform procedures; and (4) we incorporated fully-sampled

single-dish CO data into the BIMA SONG maps for over half of the galaxies, so that all CO flux is included for these galaxies.

In this paper, we address one fundamental aspect of the molecular gas distribution in galaxies: what is the radial surface brightness distribution of molecular gas, and how does it compare to that of the stars? Because stars form from molecular gas, the molecular disk in a galaxy and the stellar disk, where the bulk of the new stars reside, should have related radial distributions. In fact, Young & Scoville (1982) used single dish observations to show that, in the two galaxies they studied, the single dish radial profile and the optical B-band profile had very similar scale lengths. On the other hand, Sakamoto et al. (1999a) derived a $1/e$ length of only 500 pc for their sample; this is a small fraction of the stellar light scale length. Sakamoto et al. (1999a) compared their data with results from single-dish studies of the same galaxies and suggested that they were detecting a central CO concentration distinct from the large-scale gas disk.

In order to compare the radial distributions of molecular gas and star formation over a range of radii and size scales, we have chosen a subsample of 15 BIMA SONG galaxies for which we currently have near infrared or optical images and for which we have incorporated single-dish data into the BIMA SONG maps. We find that the CO distributions for most of the galaxies show significant deviations from the stellar disks on both large ($\sim 60''$ or more) and small ($\sim 6''$) scales. We also find that in over half of the galaxies, the CO surface brightness increases in the central kiloparsec in a similar fashion to the increase in the stellar surface brightness caused by the bulge stars. This increase may either represent a true increase in the molecular mass or it may instead represent an increase in the emissivity of the CO.

2. BIMA SONG Sample Selection

We selected galaxies for the complete BIMA SONG sample using criteria which are not explicitly based on the CO luminosity of the galaxies. The galaxies were selected to have Hubble types between Sa and Sd with a recessional velocity $v_\odot < 2000$ km s^{-1}; if H_0=75 km s^{-1} Mpc^{-1}, this corresponds to galaxies with Hubble distances of $d \lesssim 27$ Mpc. The galaxy inclinations are all $<70^\circ$(based on axial ratios) so that we may study properties which vary azimuthally. A minimum declination of -20° ensures that the sources can be observed well from the Hat Creek Radio Observatory in northern California. Finally, to limit the size of the sample, we chose galaxies with apparent blue magnitudes brighter than 11.0. Using

the NASA/IPAC Extragalactic Database (NED)[10] we identified 45 galaxies meeting these criteria. All except M33 were observed, yielding a sample size of 44 galaxies for BIMA SONG. At the average distance of the sample (∼11 Mpc), our nominal synthesized beam of 6″ provides a linear resolution of 330 pc. Table 1 lists the galaxies selected for the BIMA SONG survey.

For this paper, we selected galaxies for which we have an optical or near-infrared image as well as a single dish CO map from the NRAO 12m telescope. The subsample (Table 2) tends to be biased towards the brighter CO galaxies in the full BIMA SONG sample, but its distribution in Hubble type (Sab-Scd) and bar type (7 or 47% are classified as SAB or SB, vs. 24 or 54% in the full sample) is representative of the full sample. None of the galaxies in this first subsample is significantly distorted or asymmetric, as might be expected in strongly interacting systems. The subsample does include galaxies which are weakly interacting or have smaller companions, such as NGC 3627, NGC 5055, NGC 5194 (M51), and NGC 7331.

3. Observations

3.1. BIMA Observations

We carried out BIMA SONG observations from November 1997 through June 1999 using the 10-element Berkeley-Illinois-Maryland Association (BIMA) millimeter interferometer (Welch et al. 1996) at Hat Creek, CA. We made the observations using the C and D array configurations, which include baselines as short as 7.6m (with the 6.1m BIMA antennas as closely spaced as possible) and as long as 90m. We observed two-thirds of the galaxies (those with $R_{25} > 200''$) using a 7-field, hexagonal mosaic with a spacing of 44″; this pattern yields a half-power field of view of about 190″, or 10 kpc, at the average distance of galaxies in the survey. We observed the remaining galaxies with a single pointing, which yielded a field of view of 100″ FWHM. We observed some galaxies (NGC 0628, NGC 1068, NGC 2903, NGC 3627, NGC 4736 (Wong & Blitz 2000), NGC 5033 (Wong 2000), & NGC 5194) with slightly different pointing spacings or additional fields. For the multiple-pointing observations, we observed each field for one minute before we switched to the next pointing. Thus, we returned to each pointing after ∼8 minutes, which is well within the time needed to ensure excellent sampling of even the longest baselines in the uv plane. (For a 100″ source, the time to cross an individual uv cell at 6″ resolution is about 48 minutes; see Welch 1993.) We

[10]NED is operated by the Jet Propulsion Laboratory, Caltech, under contract with the National Aeronautics and Space Administration.

configured the correlator to have a resolution of 1.56 MHz (4 km s^{-1}) over a total bandwidth of 368 MHz (960 km s^{-1}).

3.2. NRAO 12m Observations

We collected single-dish data over several observing seasons from 1998 April through 2000 June using the NRAO[11] 12m telescope on Kitt Peak, AZ. We observed orthogonal polarizations using two 256 channel filterbanks at a spectral resolution of 2 MHz (5 km s^{-1}), and using a 600 MHz configuration of the digital millimeter autocorrelator with 0.8 MHz (2 km s^{-1}) resolution as a redundant backend on each polarization. We monitored the pointing every 1-2 hours with observations of planets and strong quasars. We also measured the focus at the beginning of each session and after periods during which the dish was heating or cooling.

In order to minimize relative calibration errors and pointing errors across the map, we observed in On-the-Fly (OTF) mode (Emerson 1996), where the telescope takes data continuously as it slews across the source. In this mode, the actual telescope encoder positions are read out every 0.01 seconds and folded into the spectra, which are read out every 0.1 seconds. Each $6' \times 6'$ OTF map takes $<$20 minutes to complete, and each source needed 10 to 30 OTF maps to achieve the desired sensitivity. (Following Cornwell, Holdaway & Uson (1993), we tried to spend enough time on the single-dish measurements to match the signal-to-noise ratio of the interferometric observations. In practice, the BIMA maps tended to have better noise levels by a factor of about two) Given reasonably stable observing conditions, the relative flux calibration across an individual map will be very good, so that even if the absolute flux scale drifts from map to map, the combined final 12m map will have very good pixel-to-pixel calibration. A careful analysis of well-pointed data (§4.2.1) over many observing seasons shows that the absolute flux calibration at the 12m is accurate to better than 10%. We weighted and gridded the OTF data to an $18''$ cell in AIPS.

3.3. Optical/Infrared Observations & Calibration

The optical or near-infrared images used in this paper were taken either from the literature or from a set of observations which were taken to form a complementary database

[11]The National Radio Astronomy Observatory is operated by the Associated Universities, Inc., under cooperative agreement with the National Science Foundation.

of broad-band images for SONG galaxies. Table 3 summarizes the data used for each of the galaxies presented in this paper.

We observed NGC 3351 and NGC 4321 using the Dupont 2.5m at Las Campanas in May of 1998 in non-photometric conditions. We used the wide field reimaging camera with the TEK5 chip yielding a plate scale of $0\overset{''}{.}7$ per pixel. These were calibrated using published aperture photometry values. We observed NGC 4258 and NGC 4736 using the 0.9m at Kitt Peak in April of 1999 in photometric conditions. We used the T2KA chip in direct imaging mode, which yielded a plate scale of $0\overset{''}{.}38$ per pixel. Finally, we observed NGC 4826 using the 1.5m at Palomar Observatory in April of 2000 in photometric conditions. The plate scale of the images after using on-chip 2x2 binning was $0\overset{''}{.}78$ per pixel. For all of the observing runs, the data were flat fielded, cosmic ray rejected, and sky subtracted using standard IRAF routines.

4. CO Data Reduction and Calibration

4.1. Reduction of BIMA data

We conducted the BIMA CO data reduction using standard tasks available in the MIRIAD package (Sault, Teuben, & Wright 1995). We removed the instrumental and atmospheric phase variations from the source visibilities by referencing the phase to observations of a nearby quasar every 30 minutes. We measured and removed the antenna-based amplitude and phase variations as a function of frequency, using the BIMA online passband observations at the time of each track. After inspecting our observations of our primary flux calibrators for any residual, baseline-based passband errors, we concluded that no further passband corrections were necessary.

We detected continuum emission in NGC 1068 and NGC 3031. For these sources, we subtracted the continuum in the visibility plane by fitting a constant to the real and imaginary parts of those channels in the passband that were free of line emission. The continuum maps derived in this way were consistent with maps made from the line-free lower sideband of the local oscillator at 112 GHz.

Additional steps in the data reduction process for BIMA SONG data, customized to ensure uniformity across the BIMA SONG sample, are described in the following subsections. A detailed description of specific imaging and data combination techniques will be presented in Helfer et al. (2001).

4.1.1. Atmospheric Decorrelation Correction

Differences in the column of water vapor between a pair of antennas are a source of phase noise that increases with increasing baseline length. This phase noise results in a decorrelation or reduction in the measured visibility amplitude, which distorts the high-resolution map structure. We made estimates of the decorrelation using measurements taken by the real-time phase monitor (Lay 1999) at Hat Creek. The phase monitor reports the rms phase variation over a fixed baseline of 100m every 10 minutes based on observations of a commercial direct broadcast satellite. We scaled the phase monitor data to our observing frequency, assumed that the phase rms scales as (baseline length)$^{5/6}$, assuming Kolmogorov turbulence (Kolmogorov 1941; Akeson 1999), and corrected for the airmass of each visibility. In general, data for which the decorrelation was large were rejected and not included in the final datasets. For the included datasets, we decreased the weight of the data according to the estimated loss in sensitivity resulting from decorrelation and scaled the visibility amplitude up according to the estimated decorrelation. This technique results in a dirty map which is essentially unchanged, but a dirty beam that more accurately represents the instantaneous atmospheric-limited response of the interferometer. It also enables a more accurate deconvolution, as the final beam size more accurately represents the degraded resolution, and produces a better estimate of the true noise level. The typical increase in beam size was only $\lesssim 5\%$, reflecting the high quality of most of the data.

4.1.2. Amplitude Calibration

We set the amplitude scale for the BIMA SONG maps using observations of the nearby quasar that was used for phase calibration. Since the flux of quasars are generally variable, we determined their fluxes by comparing them to the primary flux calibrators Mars or Uranus. In addition, we used 3C273 as a secondary calibrator. We observed one of these flux calibrators in almost every track. While the brightness temperature for the planets is generally well-determined, the flux of 3C273 is variable. To determine the flux of 3C273, we extracted observations of 3C273 from the BIMA archives and calculated the flux of 3C273 every time it was observed with a planet in any track at any frequency in the 3mm band during the period of our observations. We estimate the uncertainty in our determination of the flux of 3C273 to be less than 10%.

With these uncertainties in calibrator fluxes, measured and estimated errors in the gains at 115 GHz, and estimates of atmospheric decorrelation on time scales shorter than 10 minutes, we assign a one sigma uncertainty to our amplitude calibration of 15%.

4.1.3. Self-Calibration

Although the use of a nearby quasar to calibrate phase variations removes most of the phase errors in the observations, there can still be errors introduced by the atmospheric difference between the phase calibrator and the source and by incorrect baseline determinations. To correct for these errors, we performed an iterative phase-only multi-channel self-calibration on our source using the initial phase-calibrated map as the model for the first iteration. The model output from the deconvolution of this map was used as the input for the self-calibration, and the self-calibrated visibilities were then used to make a new map. This process was repeated for three iterations. In general, the phase gains determined by this process were small ($<20°$) and the maps were not greatly changed. We checked that the source position was not affected by self-calibration by comparing the position of the source in the self-calibrated map to its position in the *a priori* phase-calibrated map.

4.1.4. Production of BIMA CO Maps

In producing initial maps of the CO emission, we weighted the visibility data by the noise variance to account for differences in system temperatures and gains of the individual antennas. We further applied robust weighting (Briggs 1995; Briggs, Schwab & Sramek 1999; Cornwell, Braun & Briggs 1999) to the visibilities. We included shadowed data down to projected separations of 5m. For each galaxy, we smoothed the amplitude- and phase-calibrated BIMA data to 10 km s^{-1} resolution (a few narrow-line sources were smoothed to 5 km s^{-1}) and generated data cubes in right ascension, declination, and LSR velocity. We deconvolved the BIMA-only data cubes using a Steer-Dewdney-Ito CLEAN algorithm (Steer, Dewdney & Ito 1984). These BIMA-only maps were used to register pointing of the single-dish OTF maps (§4.2.1) prior to combining the BIMA and single-dish data cubes (§4.2.2).

4.2. Combination of BIMA and Single Dish Data

We have investigated several methods for combining the interferometer and single dish data in order to produce maps with no "missing" flux; the results of this analysis will be presented by Helfer et al. (2001). In this initial paper, we present maps made using a linear combination method described in Stanimirovic et al. (1999). The following subsections describe the production of these maps.

4.2.1. Pointing Cross-correlation

The implementation of OTF mapping at the NRAO 12m (§3.2) ensures that the internal pointing consistency of an individual map (taken over ∼20 min) is excellent, even if the overall registration of the map is uncertain. We were further able to cross-correlate either the individual OTF maps or averages of several maps with each other to track relative pointing shifts, allowing OTF maps taken over many hours, days, or even in different observing seasons to have good internal pointing accuracy. The absolute registration of the 12m maps was accomplished by cross-correlating the well-pointed average 12m map with the BIMA map, where the BIMA map was smoothed to match the 55″ resolution of the 12m at 115 GHz. (In performing this cross-correlation, we must assume that the flux resolved out in the interferometer maps does not affect the centroid of the emission. A theoretically more robust method, comparing flux density just in the region of *uv* overlap, is limited by poor signal-to-noise ratios.) We used the pointing cross-correlation to correct the registration of the 12m maps. In general, these corrections were 5-10″ but some were as large as ∼20″.

4.2.2. Interferometer and Single Dish Combination

Using the Stanimirovic et al. (1999) method, we created a new "dirty" map by a linear combination of the interferometer map (prior to CLEANing) and the single dish map, with the latter tapered by the primary beam response of the BIMA map (for a mosaic this is the combined response of the individual pointings). In performing this combination, the single dish map was downweighted according to the ratio of the area of the BIMA beam to the area of the 12m beam (typically about 0.01), and a new dirty beam was created by linearly combining the synthesized BIMA beam and the 12m beam (assumed to be a truncated Gaussian) using the same relative weighting.

We then deconvolved the new combined "dirty" map in the usual way using a Steer-Dewdney-Ito CLEAN algorithm. Hereafter, the cleaned maps resulting from this technique are called "BIMA+12m" or combined maps.

4.2.3. Production of Integrated Intensity Maps

To create images that best show the total integrated emission from each galaxy, we formed moment maps using a smoothed version of the data cube as a mask. We formed the mask by smoothing the data by a Gaussian with FWHM=20″ and then accepting all pixels in each channel map where the emission in the smoothed data cube was above three times

the noise. (We calculated the noise in emission-free channels of the smoothed cube). The moment map was then the sum of all emission in the accepted pixels of the full-resolution cube, multiplied by the velocity width of an individual channel. Although this technique is sensitive to low-level emission distributed similarly to the bright emission, it introduces a bias against compact, faint emission which is distributed differently than the brightest emission. Figure 1 (left hand column) shows the relationship between the CO and stellar morphologies by overlaying the CO emission distributions on our near infrared/optical images of the galaxies. The total emission (moment 0) images for the galaxies are shown separately in Figure 1 (right hand column). For all quantitative analyses in this paper, we used moment maps made without any masking to avoid the potential bias described above.

5. Results

5.1. Molecular Gas Distributions

The 15 maps shown in Figure 1 (right hand column) reveal a variety of molecular morphologies that are representative of the BIMA SONG sample as a whole. The FWHM of the synthesized beams is indicated in the lower left corner of the images in Figure 1 and is listed in Table 2. Structures are present in these maps at the smallest scales sampled by the observations, typically about $6''$, as well as on scales many times larger than the synthesized beams. There are grand-design spiral galaxies (NGC 0628, NGC 5194), where the CO is tightly confined to the spiral arms. These arms wind into the nuclear region, which lacks a single nuclear peak. By contrast, the molecular gas appears to be more smoothly distributed in the flocculent galaxies NGC 4414 and NGC 5055; this is at least partially due to the higher inclination of these galaxies, which produces a lower linear resolution parallel to the minor axis. The barred galaxies show a diversity of structure: in NGC 3351, the gas appears concentrated nearly entirely along the “twin peaks” area of the nuclear region (Kenney et al. 1992), whereas in NGC 3627, molecular gas is observed in a central concentration, along the leading edges of the bar, at the end of the bar, and extending over nearly $4'$ on the sky in spiral arms that extend from the ends of the bar. Although the highest CO surface brightness often occurs at or near the nucleus of the SONG galaxies, this is not universally the case: NGC 3521, NGC 4414, and NGC 7331 have a pronounced lack of emission at their centers. Furthermore, in NGC 628, NGC 1068, NGC 3351, NGC 4258, and NGC 5194 the strongest emission is not associated with the nucleus of the galaxy.

5.2. Radial Profiles of Molecular Gas

To explore the radial distributions of molecular gas, we calculated CO radial profiles from the $\sim 6''$ resolution BIMA+12m combined maps as well as the $55''$ resolution 12m OTF maps. We determined the position angles and inclinations (Table 2) from either the stellar light or from the CO kinematics and then measured the average brightness in concentric elliptical annuli for each source. We fixed the centers for all profiles at the position of the peak in the stellar maps. We used unclipped moment maps to avoid any biases against faint emission and measured the average in each annulus. Annuli were spaced at approximately one-half of the resolution of the corresponding image. Thus, the CO BIMA+12m profiles are described by data points spaced $3''$ apart and the 12m profiles are described by data points spaced $27''$ apart.

We converted CO brightnesses to logarithmic units in order to compare with stellar profiles. However, the use of a standard magnitude scale leads to difficulties at radii where the brightness approaches the noise level, since here the brightnesses can be very small or even negative (e.g., due to residual deconvolution errors). To put the data on a scale which is better behaved near the noise level of the image, we adopted a modified magnitude scale recently developed for optical studies. We used inverse hyperbolic magnitudes (Lupton, Gunn & Szalay 1999) with the zero magnitude set at 1000 Jy km s^{-1} arcsecond^{-2}. In detail, we converted to magnitude μ using

$$\mu(x) = -2.5 \log_{10}(e) \left[\sinh^{-1}\left(\frac{x}{2b}\right) + \ln b \right], \quad (1)$$

where x is the flux and b is the "softening" parameter that determines the threshold of linear behavior of the magnitudes. When x is large relative to b, these magnitudes reduce to the standard astronomical magnitude scale. Lupton, Gunn & Szalay (1999) showed that the optimum value for the softening parameter b is the noise level of the flux measurement. As the noise level of the combined maps varied little from galaxy to galaxy, the softening parameter was held constant at b=1.33 Jy km^{-1}s^{-1}beam^{-1}.

The $55''$ resolution data from the 12m telescope produce smooth, monotonically decreasing profiles that can be described by a single exponential (with the possible exception of NGC 7331). The BIMA+12m $6''$ resolution maps, on the other hand, yield complex, heterogeneous profiles, with a great deal of structure on sub-kiloparsec size scales.

5.3. Comparison of CO and Stellar Radial Profiles

Stellar profiles were produced for the optical/infrared images of our subsample galaxies in a manner similar to the CO profiles. Due to the higher resolution available at these wavelengths, points on the optical/infrared profiles are spaced $1''$ apart. In addition, we used the median intensity in each annulus to avoid surface brightness excursions caused by foreground stars.

Figure 2 compares the stellar profiles with the CO radial brightness distributions for each galaxy. The stellar profiles show the expected exponential disk plus a central de Vaucouleurs ($r^{1/4}$) bulge component. Most remarkably, in 8 of the 15 galaxies (see Table 5) in Figure 2, there appears to be a separate, bulge-like excess CO component to the BIMA+12m profiles that occurs over a radial extent roughly similar to the bulge component of stellar light. Here we classify a galaxy as having an excess CO central component when the central CO surface brightness is brighter than the extrapolation of the large scale disk to zero radius.

It would be surprising if the CO emission and bulge star light were directly related because the optical/IR bulge is the projection of a 3-dimensional distribution while the CO distribution throughout the entire galaxy is almost surely a flattened disk. Furthermore, the BIMA+12m data are, in general, not well fit by an exponential radial distribution even at radii where there is no contribution from the nucleus. Apparently, the low resolution data often mask complex radial profiles as well as large variations in the azimuthal distributions.

To compare the BIMA+12m CO surface brightness profiles and the stellar surface brightness profiles directly, we determined the average magnitude offset between the two profiles. First, we convolved the stellar images to the resolution of the CO images and sampled the stellar images at the same intervals as those of the CO images to form a matching stellar radial profile. We used this profile as input to a joint bulge/disk decomposition routine (Regan & Vogel 1994). Due to the low resolution of the convolved stellar profile in the central region, a good fit is obtained without uniquely determining the parameters of the individual bulge and disk components. From these model parameters, we then created a model stellar profile to deemphasize the deviations in the original stellar surface brightness profile caused by spiral arms, bars, and foreground stars. We determined the offset between the stellar profiles and the BIMA+12m profile by averaging the offsets at each annulus. Figure 3 shows a plot of the offset modeled stellar surface brightness profiles, the offset stellar profile, the CO BIMA+12m, and the 12m profiles. The figure shows that, although the stellar and CO profiles display a similar surface brightness distribution in some galaxies, in general, there are deviations of two magnitudes or more over a large range in radius. In some nuclei, this difference is as much as four magnitudes.

5.4. Constancy of the CO to K-band Flux Ratios

Is the qualitative agreement between the stellar surface brightness profiles and the low resolution CO surface brightness profiles evidence of a relationship between the CO flux and the stellar flux in these galaxies? For comparison, we converted all the stellar images to a K-band magnitude scale using colors determined from published aperture photometry values (see Table 3 for colors and references). The uncertainties in this calibration are the dominant source of uncertainties in the total stellar magnitudes, but they are small compared to the uncertainties of the CO flux scale (see §4.1.2). We calculated the magnitudes using the total flux inside a radius of 190″ for the single dish CO and stellar profiles. Figure 4 (upper panel) shows the resultant CO-K offset as a function of the Hubble type of the galaxies. Here a relatively brighter CO flux compared to the stellar flux results in a more negative CO-K offset. There is a trend of increasing CO luminosity relative to the stellar luminosity for later Hubble types. This increase in CO luminosity is the opposite of what was seen by Casoli et al. (1998), who found that CO emission decreases relative to dynamical mass with later Hubble types.

The trend seen in the top of Figure 4 is a semi-quantitative expression of gaseous properties of the Hubble sequence. Late-type galaxies contain more gas and dust than early-type galaxies (Sandage 1961), and the more negative CO-K offsets in the later type galaxies imply that, globally, these galaxies contain, on average, more molecular gas and, by implication, more dust than the early-type galaxies. Given that the HI surface densities saturate at an A_v of 0.5 mag (Wong 2000 and references therein), inclusion of HI, which is beyond the scope of this paper, should add to the scatter in the relation and perhaps affect the slope somewhat, but not the trend itself.

Figure 3 shows that for 8 of the 15 galaxies, the CO surface brightness increases in the bulge region in a manner similar to the stellar surface brightness. The presence or absence of a central excess is summarized in Table 5. To investigate quantitatively whether the relationship between CO luminosity and K-band flux is the same in the bulge and disk regions, we show the CO-K offsets of the bulge regions and disks as a function of Hubble type in Figure 4 (middle panel) and (bottom panel), respectively. We take one kiloparsec as the fiducial radius of the bulge and sum all the flux inside this radius, using the BIMA+12m for the CO. The remaining flux out to a radius of 190 arcseconds (from the single dish CO data) is assigned to the disk component. The flux values are shown in Table 4.

Linear regressions for all three plots in Figure 4 give similar slopes and intercepts. The slopes for the entire galaxy and the disk alone are –0.39±0.11 and –0.37±0.14 respectively; the slope for the bulge alone is –0.47±0.28 (with one sigma uncertainties). The intercept for the entire galaxy is –5.7. The fits show that there is a statistically significant relationship

between the CO-K offset and the Hubble type. The K-band light is thus a predictor of the CO flux, not only in the disk but also in the bulge, and the relationship between the two quantities is the same, within the uncertainties, both in the bulge and the disk. This is quite surprising given the large variation of emission distributions in the sample galaxies shown and the difference in geometry between the stellar and CO emission from the bulge region.

There is a significant difference between the amount of light contributed by disk stars and bulge stars in the two different regions. As one would not expect the light from bulge stars to be related to the CO emission, one would expect the CO-K offset of the bulge region to be different from that of a region where the light is dominated by disk stars. We can use our simple disk/bulge decomposition model to give us an estimate of how much of the stellar light in the inner kiloparsec arises from the bulge stars and how much comes from the disk. By averaging all fifteen galaxies, we find that the disk-only stellar light is 2.2±0.14 magnitudes fainter than the total light within the inner kiloparsec. Thus, if the CO surface brightness were related only to stars in the disk, then the CO-K offsets in the bulge region would be 2.2 magnitudes larger than the mean of the values measured for the disks in the bottom panel of Figure 4. The mean of the points in the bulge, shown in the middle panel, is, however, only 0.52±0.38 larger than what is measured for the disks of the galaxies, an increase of only marginal significance. Thus, the mean CO-K offset is very nearly the same in the bulge as in the disk, a rather surprising result given that the geometries of the two stellar components are so different.

5.5. Scale Lengths of the CO and Stellar Disks

The surprisingly good correlations between CO and K-band flux in disks suggest that the scale lengths of the two distributions in the galaxy disks might be similarly correlated. In Figure 5, we plot the scale length of the stellar disk from the optical/near-infrared image and the CO scale length determined from the low resolution CO data. In both cases we fit the slope of the surface brightness ignoring the central $50''$ to avoid the contribution from the bulge. In Table 5 we list the scale lengths and uncertainties for each galaxy. A weighted fit to the data yields a slope of 0.53±0.03 and an intercept of 0.90±.09, with a correlation coefficient of 0.50, but there is no systematic trend for either the CO or stellar disk to be longer than the other because of the non-zero intercept of the fit. This non-zero intercept is probably due to the large scatter in the data, which exceeds the measurement uncertainties. Another way to see this is to consider the mean ratio of the CO to stellar scale length, which is 0.88±0.14, with a dispersion of 0.52. The uncertainty in the mean is 16%, even though the measurement uncertainty for any one galaxy is typically less than about 10%. Thus, it

appears that the stellar and CO scale lengths for the disks in the 15 galaxies plotted are on average equal, but the relatively large scatter in the data suggest that there are real variations in the ratio from galaxy to galaxy. The equality of the scale lengths, on average, raises a question similar to that posed for the Milky Way (e.g. Blitz 1996): are the two scales lengths tied together, and if so, which controls the other? Clearly, the scale lengths often differ in an individual galaxy (see especially NGC 628), contrary to the implication of the two-galaxy study by Young & Scoville (1982).

6. Discussion

6.1. CO distributions at High and Low Resolution

At 45″ resolution, only 10 of the 193 galaxies surveyed as part of the FCRAO Extragalactic CO Survey (Young et al. 1995) exhibited rings, and 18 had peaks offset from the nucleus. Thus 15% of the FCRAO sample were inferred to have distributions which lack a central peak. Our radial profiles derived from the single-dish data are consistent with these results. Of the 15 galaxies presented in this paper, all show a single-dish radial profile which rises monotonically to the nucleus, supporting the idea that molecular gas distributions which are not concentrated with the central r $\lesssim$ 5 kpc are relatively rare.

At full resolution, however, ~50% of the SONG subsample galaxies do not exhibit peaks at the center. This disparity with the low resolution results is unlikely to be due to the selection of galaxies. The different conclusions regarding central CO peaks derived from the FCRAO and SONG surveys are unlikely to be due primarily to differences in the samples. Indeed, if we considered only our own (slightly lower than FCRAO resolution) 12-meter data, we would conclude that for nearly all galaxies the peak CO emission occurs at the center. With the benefit of higher angular resolution, we find that for at least 50% of the SONG sample, the peak CO emission is not at the center. In other words, with linear resolution on the order of a few 100 pc, only in roughly half the galaxies does CO peak at the center. Thus, this analysis demonstrates the importance of high-resolution observations of molecular gas and suggests that the conventional view that molecular gas generally peaks at the nucleus is incorrect.

6.2. Radial Distribution of CO

Probably the most striking feature in both the radial profile plots (Figure 2) and the plots of CO-K offsets (Figure 4 upper panel and middle panel) is the relationship between the

surface brightness of the bulge and the surface brightness of the molecular gas as measured by the CO surface brightness. For all eight galaxies that show an excess of CO emission above the exponential disk profile in their central regions, the excess is strikingly similar to the increase in the stellar light due to the bulge component. The bulge component of the stellar radial profile is generally attributed to a flattened spheroid. On the other hand, the molecular gas distribution almost certainly remains disk-like; the gas is highly dissipative and the kinematics show regular rotation to first order. Thus, it is striking that the BIMA+12m profiles cannot, in general, be fitted by a single exponential profile over all radii, and that furthermore, many deviate from an exponential profile at approximately the same radii as the central stellar bulge component starts to dominate. This is true not only for strongly barred galaxies, such as NGC 2903 and NGC 3627, but also for unbarred galaxies such as NGC 5055.

6.3. CO Emission Excesses in the Centers of Galaxies

We consider two possibilities for the observed excess of CO emission in the bulge region. The two are not mutually exclusive and may, in fact, be related. The first involves the hydrostatic pressure of gas in the bulge. The second, assume that the bulge has, in fact, formed from the molecular gas in the nuclear regions of the galaxy.

For the bulge stars to be able to influence the molecular gas near the galaxy center, there must be a mechanism to transport information about the gravitational potential to the molecular disk. If there were a hot gas in the bulge region of these galaxies with a filling factor approaching one, then it would provide a mechanism for influencing the disk gas by increasing the pressure in the bulge region. Spergel & Blitz (1992) show that the observed X-ray emitting gas in the Milky Way will translate the gravitational potential of the bulge into an increased pressure in the center of the Milky Way. This increased pressure leads to an increase in the average density of the gas compared to the local value (Helfer & Blitz 1997b) and to an increase in the internal velocity dispersion of the clouds (Bally et al. 1987). This increased density has also been seen in the bulge regions of other external galaxies (Helfer & Blitz 1997a). Given the different environment in the bulge regions, could this influence the conversion factor of CO luminosity to H_2 mass, X, which has been determined locally?

From the analysis of Maloney & Black (1988) there are three interacting effects that will change the relationship between CO luminosity and H_2 mass: kinetic temperature, T, density, ρ, and velocity dispersion increase over virial. The interaction is such that

$$X = T^{-1}\rho^{1/2}(\sigma_{virial}/\sigma_{rms})^2. \qquad (2)$$

A decrease in X indicates that the CO is more luminous for the same H_2 mass. If we look at some typical values in the center of the Milky Way, the clouds are five times hotter, 10 times denser, and have velocity dispersions around 10 times higher than local clouds (Bally et al. 1987). This increase in the density by a factor of 10 leads to an increase of a factor of $\sqrt{10}$ in the virial velocity dispersion. Therefore, we get X_{bulge}/X_{local}=0.06.

In other words, the conditions in regions like the Galactic center would cause the CO to be overluminous by a factor of 16, or 3 magnitudes, which is not far from the 2.2 magnitudes that would be required for the molecular gas surface density to follow the disk stellar surface brightness (§5.4). This is in qualitative agreement with the deficit of gamma-rays at the center of the Milky Way (Blitz et al. 1985) as well as the low value of X derived from dust measurements at the center of the Milky Way (Sodroski et al. 1995) and in three BIMA SONG galaxies (Regan 2000).

It is worth noting that two (NGC 4414 and NGC 628) of the three galaxies with the latest Hubble type show no increase in surface brightness above an exponential profile in their centers. The galaxy with the latest Hubble type in the subsample, NGC 6946, does show an excess but it is also undergoing a nuclear starburst which could provide an excess pressure through a large number of supernovae. Spergel & Blitz (1992) predicted that the smaller bulges of late type galaxies would give rise to lower interstellar gas pressures than earlier types. This would lead us to expect that later Hubble type galaxies would not have as large of an excess of CO emission in their central regions.

This interpretation of the cause of the excess CO emission in the nuclear region of some of these galaxies could be tested by high resolution millimeter observations of individual clouds in the bulge regions of one of the galaxies with a central excess. If the clouds show a large internal velocity dispersion, similar to clouds in the bulge region of the Milky Way, it could account for their brighter central emission.

Another explanation for a concomitant increase in the CO and stellar surface brightness in the nuclear regions is related to a suggestion by Kormendy (1993) that at least some bulges are really disk-like ("pseudo-bulges") and form from the nuclear disk gas. These bulges have much smaller velocity dispersions than predicted by the Faber-Jackson relation (Faber & Jackson 1976) and relatively rapid rotation, suggesting that they are rotationally flattened. One of the prototype disk-like bulges mentioned by Kormendy (1993) is NGC 4736, one of the galaxies in our sample that shows a nuclear increase in the CO surface brightness in the bulge region. In this scenario, gas is brought to the center by means of a bar or some other transport mechanism and, if the gas is continually supplied, then the stars that form will have disk kinematics. If these stars are efficiently scattered by either a bar, molecular clouds in the disk, or a bending instability (Raha et al. 1991; Combes & Sanders

1981) then they can form themselves into the high angular momentum bulge that is seen in some cases. Incidentally, the high pressures in the bulge region will continue to keep the gas substantially molecular, as discussed above, which can permit continued star formation as long as the gas supply holds out. If a steady state is reached, then it would be natural for the K band to CO surface densities to have values similar to the disks; all that would be required is a near-constant star formation efficiency from the molecular gas in both regions.

One straightforward test of this hypothesis for the galaxies in our sample would require that all of the galaxies that show a CO excess in the bulge region ought to exhibit relatively high angular momentum pseudo-bulges. A second test would show metallicities inconsistent with a closed-box evolutionary model of the star formation for these bulges.

6.4. Comparison with Previous Results

A good agreement between the large scale radial distribution of the CO gas and the stellar disk was first noted by Young & Scoville (1982) for NGC 6946 and IC 342. Their under-sampled major and minor axis profiles (with an effective resolution of $> 50''$) were in very good agreement with optical B-band radial profiles. Although the central pointing of their observations did show an excess similar to what our profiles show, they concentrated their discussion on the agreement between the scale length of the CO profiles (excluding the central pointing) and the B-band disk scale lengths. Even at their $50''$ resolution, the IC 342 CO scale length agreed better with the B-band scale length when they excluded the inner three pointings, showing that the excess central emission affects even single dish profiles. Our results in Figure 5 show considerably more scatter in the relationship between the scale lengths of the CO and stellar disks than those suggested by Young & Scoville (1982).

Observations out to a radius of $30''$ of galaxies using the OVRO and NRO interferometers were made by Sakamoto et al. (1999a), who found that the CO radial profiles decreased at a rate such that the surface brightness is $1/e$ of the central surface brightness at an average distance of 500 pc. This is a much shorter distance than that found by single dish observations (Young & Scoville 1982, 1991; Young et al. 1995). In addition, by requiring a minimum surface brightness in the FCRAO survey, the Sakamoto et al. (1999a) sample may have emphasized galaxies with centrally concentrated CO distributions. By comparing the Sakamoto et al. (1999a) results with the radial profiles presented in Figures 2 and 3 of this paper, it is apparent that in such centrally concentrated galaxies, the region enclosed by r=$30''$ is essentially the bulge region that we find to be characterized by an excess of emission over the stellar disk (§5.1). While it is possible to represent the CO by an exponential in this nuclear region, it is probably completely decoupled from the larger-scale exponential that

characterizes the stellar disk.

Previous single dish studies have also suggested that the CO surface brightness varies by only a factor of two at a given radius (Young & Scoville 1982, 1991). In contrast, the high-resolution BIMA SONG maps demonstrate azimuthal variations of greater than 10 in many galaxies (for example: NGC 5194, NGC 6946, NGC 628). The distribution on small scales is inherently different than the stars in that the CO is much more clumpy. Although variations in the stellar surface brightness due to non-axisymmetric features in the disk (e.g., bars and spiral arms) can be quite strong in the vicinity of such features ($\sim$ a factor of 2), when the emission is averaged in annuli, the stellar radial profiles show only slight variations from an exponential profile. On the other hand, the CO distributions in most galaxies show large variations from exponential profiles; as the molecular gas is dynamically cold it responds strongly to perturbations such as bars, spiral arms, and resonances.

6.5. Spatial and Temporal Variations in the Disk Distribution

The average ratio of the scale lengths of the stellar and CO disks among the 15 galaxies in our sample is close to unity, suggesting that the two components are closely coupled. This agreement may be a sign that the scale lengths of both components averaged over time are the same within each individual galaxy. Even though the ratio of CO and stellar light scale lengths shows substantial differences between individual galaxies, a sample average close to unity suggests that these differences average out over time, perhaps through some feedback mechanism that suppresses the variations. One feedback mechanism that originates in the molecular gas might be the formation of new stars. As new stars form from the molecular gas they would have a radial distribution similar to the molecular gas. Over time, even if the the stellar disk started with a different scale length, it would tend toward a scale length similar to that of the molecular gas. If this were true, one prediction is that the scale of a tracer of current star formation such as Hα or U-band would have a scale length closer to the molecular gas scale length than the stellar scale length. Alternatively, if the gravitational potential of the stellar disk exerted some feedback on the molecular disk, the stellar disk could damp out variations in the molecular disk. In this way, the stars in the disk could prevent the molecular disk from diverging significantly from the stellar radial profile.

The CO distributions are much more variable than the stellar disks, in both the azimuthal and radial directions; this is a consequence of the lower random motions of the molecular gas, which makes it respond more to gravitational perturbations such as bars and spiral arms. In addition, the molecular gas in a galaxy can be depleted by the formation of new stars (either directly or by photodisassociation) and can be created out of atomic gas.

Thus, while the stellar content of a galaxy can only increase with time, the molecular gas content of a galaxy can rise and fall. The combination of these two effects can explain the variable morphology of these molecular distributions.

7. Conclusions

We introduced the BIMA Survey of Nearby Galaxies with a study of the CO radial brightness distributions of a subsample of 15 spiral galaxies. Our conclusions are:

(1) The BIMA SONG maps display a variety of distributions of molecular gas. They are considerably more heterogeneous on sub-kiloparsec size scales than are their stellar counterparts, both within a galaxy and from source to source.

(2) The radial brightness distributions of CO emission reflect the clumpy nature of the molecular gas distributions on size scales of a few hundred parsecs. This is unlike the stellar radial profiles, which tend to be smooth even on small scales despite significant contrasts in the azimuthal light distribution due to perturbations such as bars and spiral arms.

(3) The CO radial profiles cannot be explained by a single-component exponential disk model. In fact, in a majority of the galaxies the CO profiles seem to follow the two-component (bulge + disk) stellar brightness distribution quite well. The average ratio of the CO to stellar scale lengths in the disks is 0.88 ± 0.14, or close to unity, even though the dispersion (0.52) in the ratio is large enough to imply real variations from galaxy to galaxy. This may indicate that the CO and stellar scale lengths for any given galaxy are the same when averaged over time.

(4) The ratios of the CO to K-band surface brightness in the galaxies as a whole, the bulge regions, and the disk regions show a weak relationship with Hubble type. The ratio of the bulges alone is only marginally larger than for the disks, 0.52 ± 0.38 mag, much smaller than the value of 2.2 mag expected from the inward extrapolation of the disk. This implies a possible physical connection between the the bulge and the inner CO surface brightness.

(5) The excess CO emission seen in the central regions of many of the galaxies may either be due to an accumulation of molecular gas in the nuclear region or it may explained by an increase in the external pressure on the molecular clouds in the bulge region from a hot diffuse gas. This increased pressure not only raises the density but raises the internal velocity dispersion of the gas, increasing the CO luminosity relative to the H_2 mass.

The authors thank Rick Forster and the staff of the Hat Creek Radio Observatory at

Hat Creek for their help with the BIMA observations, and we thank the BIMA Board for dedicating so much time to this Observatory project. We thank Peter Teuben for assistance with the software and for many helpful discussions. We thank Peter Guarnieri for his help with the reduction of the optical data, and Annette Ferguson for providing the R band images of NGC 628 and NGC 7331 for use in this analysis. We would also like to thank the referee, Jeff Kenney, for his helpful comments on the paper. This research was supported by NSF grants AST-9981308 (UC Berkeley), AST-9981289 (University of Maryland), and AST-9900789 (Steward Observatory).

REFERENCES

Akeson, R. L. 1999, BIMA Memorandum #68

Aalto, S., Booth, R. S., Black, J. H. & Johansson, L. E. B. 1995, A&A, 300, 369

Aaronson, M. 1977, Ph.D. Thesis, Harvard University

Bally, J., Stark, A. A., Wilson, R. W. & Henkel, C. 1987, ApJS, 65, 13

Blitz, L., Bloemen, J.B.G.M., Hermsen, W., and Bania, T. 1985, å, 143, 267

Blitz, L. 1993, in Proto-Planets III, ed. E. H. Levy and J. I. Lunine, University of Arizona Press, Tucson, 125

Blitz, L. 1996, in 25 Years of Millimeter Wave Spectroscopy, ed. W.B. Latter, S.J.E. Radford, P.R. Jewell, J.G.Mangum, & J. Bally, (Dordrecht:Kluwer), 11

Boroson, T. A., Strom, K. M. & Strom, S. E. 1983, ApJ, 274, 39

Briggs, D. S. 1995, American Astronomical Society Meeting, 187, 111202

Briggs, D. S., Schwab, F. R. & Sramek, R. A. 1999, ASP Conf. Ser. 180: Synthesis Imaging in Radio Astronomy II, 127

Casoli, F. et al. 1998, A&A, 331, 451

Combes, F. & Sanders, R. H. 1981, A&A, 96, 164

Cornwell, T., Braun, R. & Briggs, D. S. 1999, ASP Conf. Ser. 180: Synthesis Imaging in Radio Astronomy II, 151

Cornwell, T. J. Holdaway, M. A. & Uson, J. M. 1993, A&A, 271, 697

Ellis, R. S., Gondhalekar, P. M. & Efstathiou, G. 1982, MNRAS, 201, 223

Emerson, D. T. 1996, in IAU symposium 170, ed. W. B. Latter, S. J. E. Radford, P. R. Jewell, J. G. Mangum, & J. Bally (Kluwer), 207

Faber, S.M., and Jackson, R.E. 1976, ApJ, 204 668

Feldmeier, J. J., Ciardullo, R. & Jacoby, G. H. 1997, ApJ, 479, 231

Ferguson, A. M. N., Wyse, R. F. G., Gallagher, J. S. & Hunter, D. A. 1998, ApJ, 506, L19

Ferrarese, L. et. al. 1996, ApJ, 464, 568

Friedli, D. & Benz, W. 1995, A&A, 301, 649

Friedli, D. & Martinet, L. 1993, A&A, 277, 27

Glass, I. S. 1976, MNRAS, 175, 191

Graham, J. A. et al. 1997, ApJ, 477, 535

Gruendl, R. A. 1996, Ph.D. Dissertation, University of Maryland

Helfer, T. T. et al. 2001, in prep.

Helfer, T. T. & Blitz, L. 1997a, ApJ, 478, 162

Helfer, T. T. & Blitz, L. 1997b, ApJ, 478, 233

Hughes, S. M. et al. 1998, ApJ, 501, 32

Jogee, S. 1999, Ph.D. Thesis, Yale University

Johnson, H. L. 1966, ApJ, 143, 187

Kenney, J. D. P., Wilson, C. D., Scoville, N. Z., Devereux, N. A. & Young, J. S. 1992, ApJ, 395, L79

Kolomogorov, A. N. 1941, ANSSSR, 30, 301

Kormendy, J. 1993, in "Galactic Bulges", H. Dejonghe & H.J. Habing, eds., Kluwer: Dordrecht, p.209

Lay, O. 1999, BIMA Memorandum #72

Lupton, R. H., Gunn, J. E. & Szalay, A. S. 1999, AJ, 118, 1406

Maloney, P. & Black, J. H. 1988, ApJ, 325, 389

Maoz, E., Newman, J. A., Ferrarese, L., Stetson, P. B., Zepf, S. E., Davis, M., Freedman, W. L. & Madore, B. F. 1999, Nature, 401, 351

Norman, C. A., Sellwood, J. A. & Hasan, H. 1996, ApJ, 462, 114

Planesas, P., Colina, L. & Perez-Olea, D. 1997, A&A, 325, 81

Raha, N., Sellwood, J. A., James, R. A., & Kahn, F. D. 1991, Nature, 352, 411

Regan, M.W. 2000, ApJ, 541, 142

Regan, M. W. & Elmegreen, D. M. 1997, AJ, 114, 965

Regan, M. W., Sheth, K. & Vogel, S. N. 1999, ApJ, 526, 97

Regan, M. W., Teuben, P. J., Vogel, S. N. & van der Hulst, T. 1996, AJ, 112, 2549

Regan, M. W. & Vogel, S. N. 1994, ApJ, 434, 536

Saha, A., Sandage, A., Tammann, G. A., Labhardt, L., Macchetto, F. D. & Panagia, N. 1999, ApJ, 522, 802

Sakamoto, K. , Okumura, S. K., Ishizuki, S. & Scoville, N. Z. 1999a, ApJS, 124, 403

Sakamoto, K. , Okumura, S. K., Ishizuki, S. & Scoville, N. Z. 1999b, ApJ, 525, 691

Sandage, A. 1961, The Hubble Atlas of Galaxies, Washington: Carnegie Institution

Sault, R.J., Teuben, P.J., & Wright, M.C.H. 1995, in Astronomical Data Analysis Software and Systems IV, eds. R.A. Shaw, H.E.Payne, & J.J.E. Hayes, A.S.P. Conference Series 77, 433

Sheth, K., Regan, M. W., Vogel, S. N. & Teuben, P. J. 2000, ApJ, 532, 221

Scoville, N. Z., Thakkar, D., Carlstrom, J. E. & Sargent, A. I. 1993, ApJ, 404, L59

Sodroski, T. J. et al. 1995, ApJ, 452, 262

Spergel, D. N. & Blitz, L. 1992, Nature, 357, 665

Stanimirovic, S., Staveley-Smith, L., Dickey, J.M., Sault, R.J., & Snowden, S. 1999, MNRAS, 302, 417

Steer, D. G., Dewdney, P E. & Ito, M. R. 1984, A&A, 137, 159

Steinmetz, M. & Muller, E. 1995, MNRAS, 276, 549

Thornley, M. D. 1996, ApJ, 469, L45

Tifft, W. 1961, AJ, 66, 390

Turner, A. et al. 1998, ApJ, 505, 297

Tully, R. B. 1988, Nearby Galaxies Catalog (Cambridge: Cambridge Univ. Press)

Verter, F. 1985, ApJS, 57, 261

Verter, F. 1990, PASP, 102, 1281

Vogel, S. N., Kulkarni, S. R. & Scoville, N. Z. 1988, Nature, 334, 402

Welch, W. J. 1993, BIMA Memorandum #32

Welch, W. J. et al. 1996, PASP, 108, 93

Wong, T. 2000, Ph.D. Dissertation, University of California at Berkeley

Wong, T. & Blitz, L. 2000, ApJ, 540, 771

Young, J. S. & Devereux, N. A. 1991, ApJ, 373, 414

Young, J. S. & Scoville, N. 1982, ApJ, 258, 467

Young, J.S. & Scoville, N.Z. 1991, ARA&A, 29, 581

Young, J. S. et al. 1995, ApJS, 98, 219

This preprint was prepared with the AAS LaTeX macros v5.0.

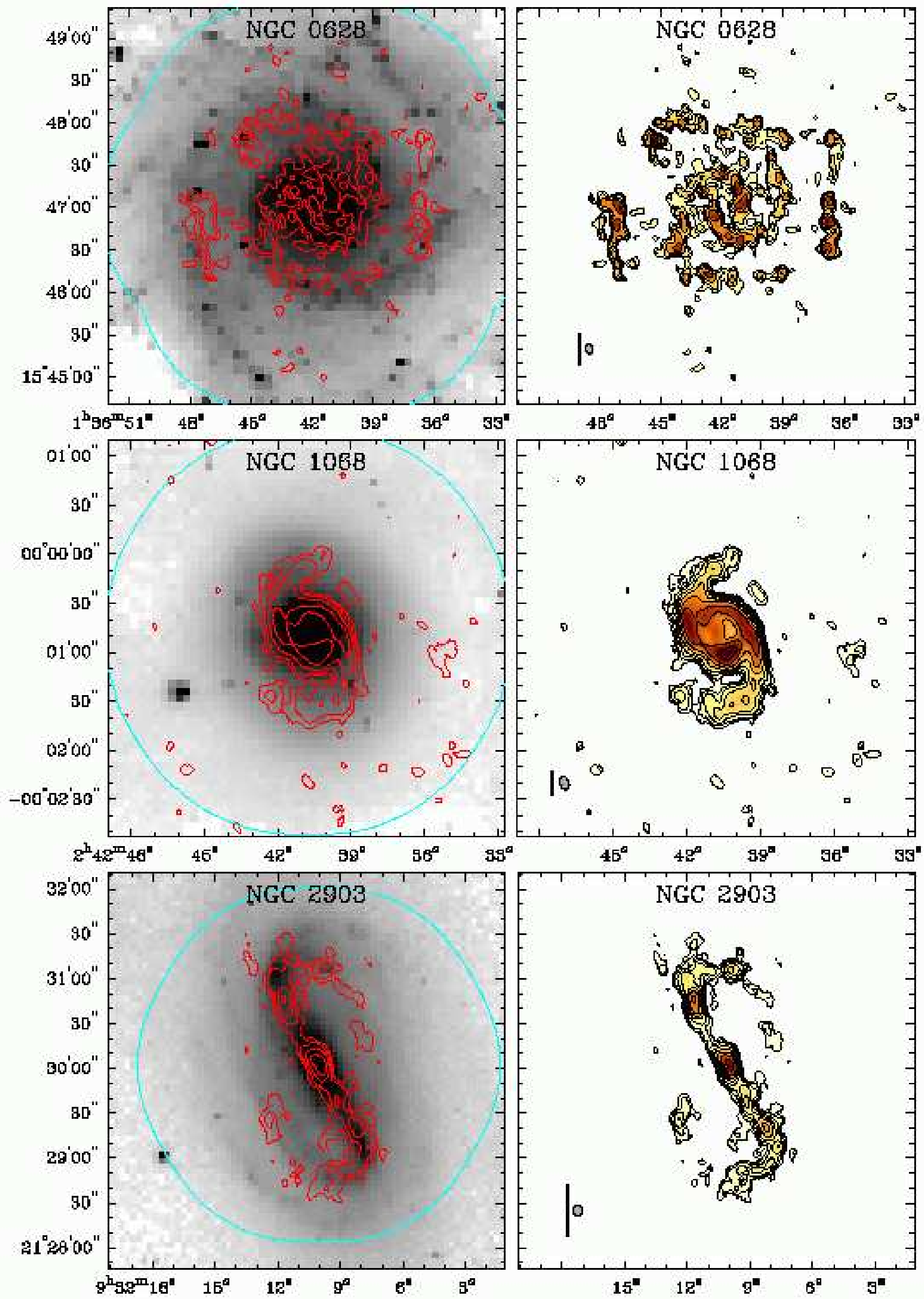
NGC 0628
NGC 0628
NGC 1068
NGC 1068
NGC 2903
NGC 2903

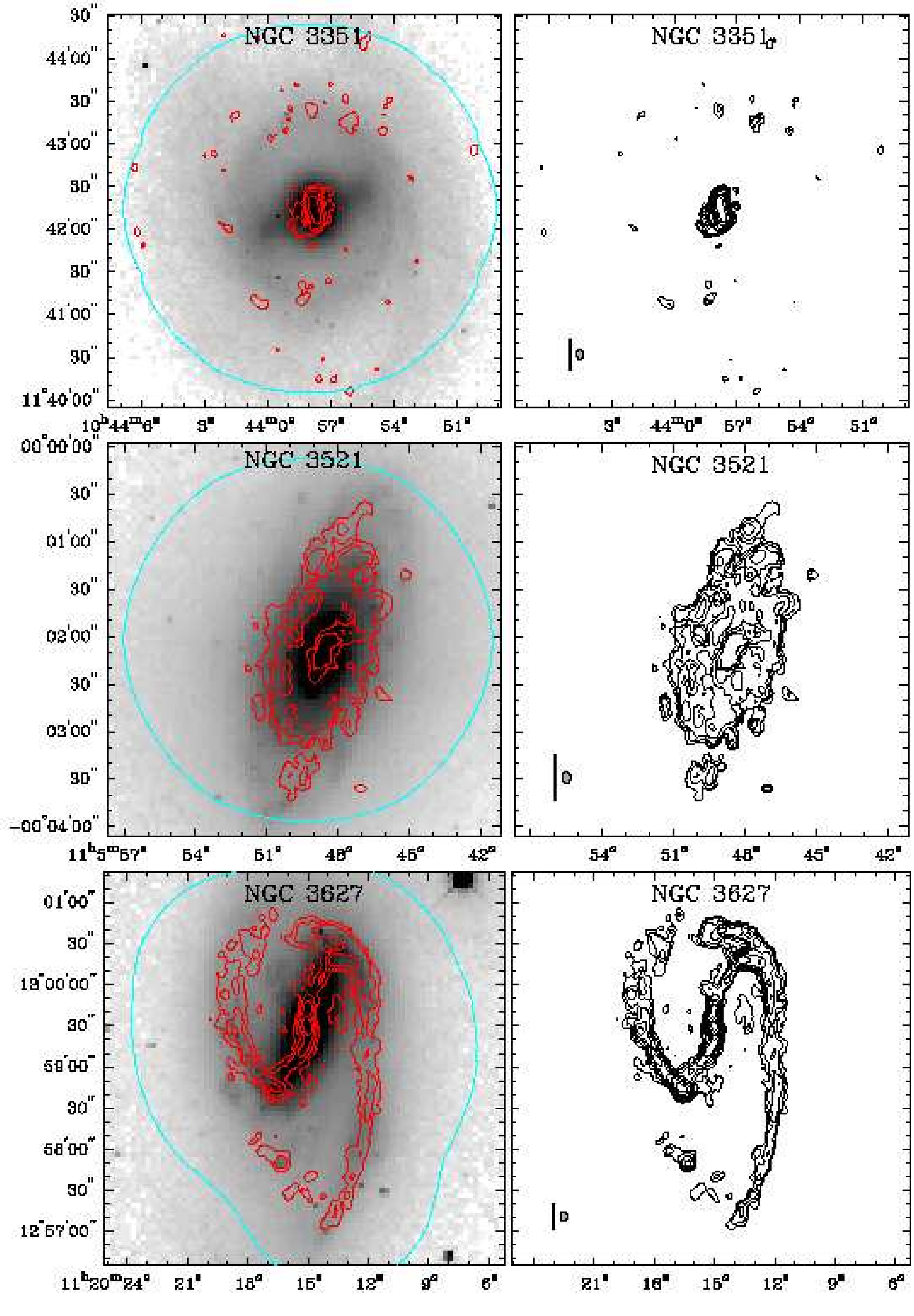
NGC 3351
NGC 3351
NGC 3521
NGC 3521
NGC 3627
NGC 3627

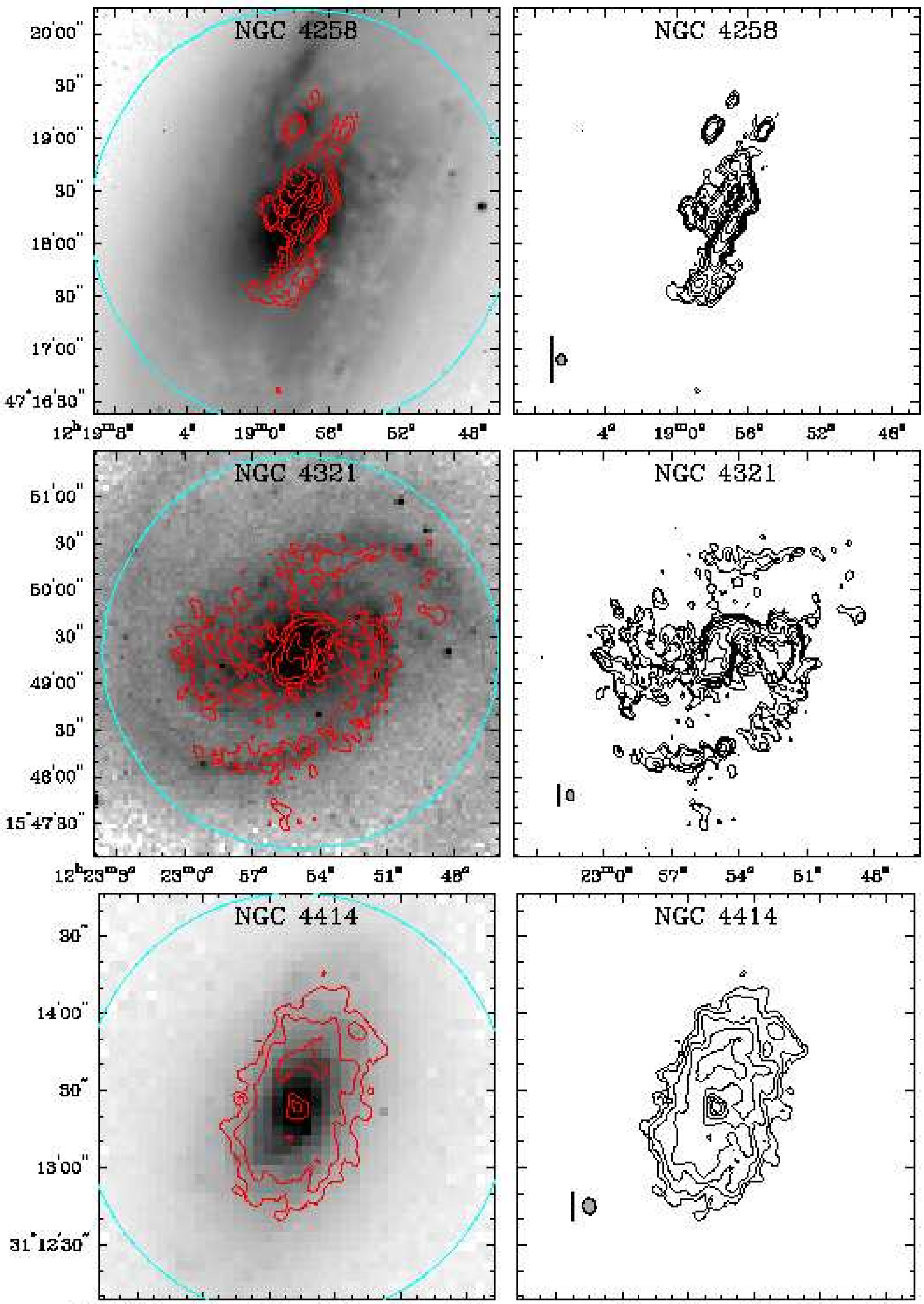
NGC 4258
20'00"
30"
19'00"
30"
18'00"
30"
17'00"
47°16'30"
12h19m8s
4s
19m0s
56s
52s
48s
NGC 4258
NGC 4321
51'00"
30"
50'00"
30"
49'00"
30"
48'00"
15°47'30"
12h23m3s
23m0s
57s
54s
51s
48s
NGC 4321
NGC 4414
30"
14'00"
30"
13'00"
31°12'30"
12h26m32s
30s
28s
26s
24s
22s
NGC 4414

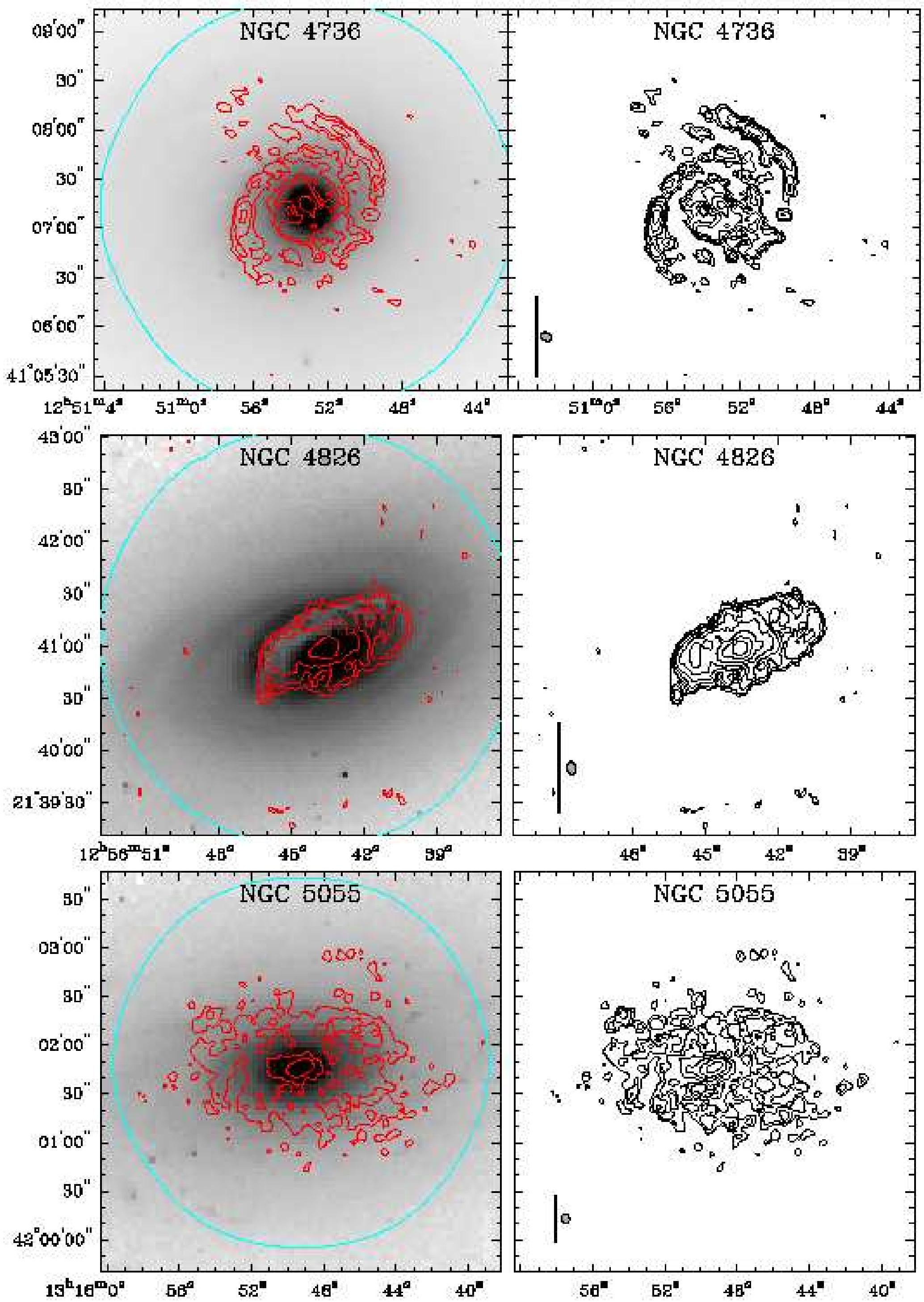
NGC 4736
NGC 4736
NGC 4826
NGC 4826
NGC 5055
NGC 5055

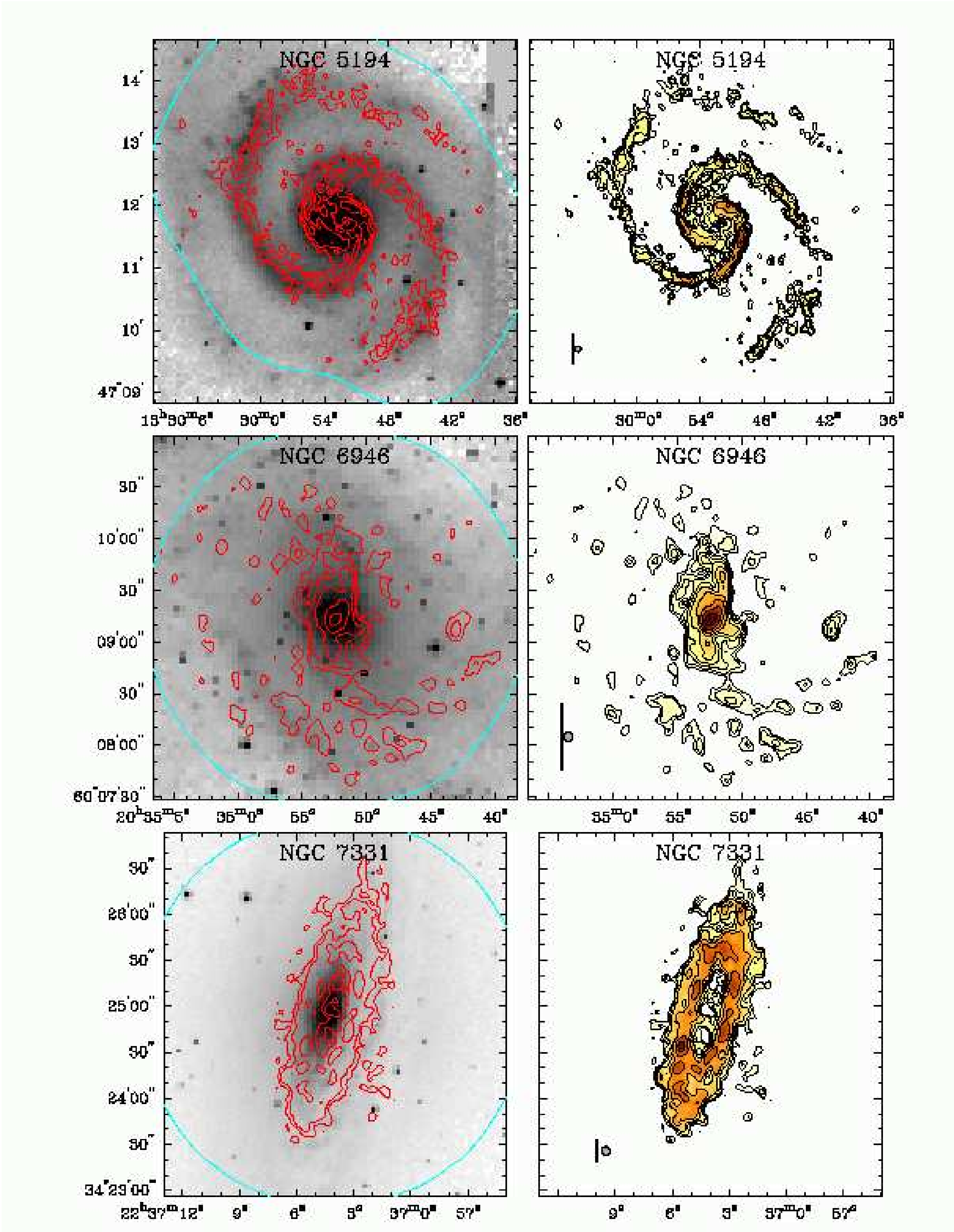
NGC 5194
NGC 5194
NGC 6946
NGC 6946
NGC 7331
NGC 7331

Fig. 1.— (left-hand column) CO contours overlaid on stellar image. The observing filter of the underlying images are listed in Table 3. Each contour is at a surface brightness of 2.5119 times higher (one magnitude) than the previous one. The starting contour levels for the galaxies are: NGC 0628 - 1.5, NGC 1068 - 6, NGC 2903 - 5, NGC 3351 - 2.5, NGC 3521 - 5, NGC 3627 - 5, NGC 4258 - 4, NGC 4321 - 3, NGC 4414 - 3, NGC 4736 - 4, NGC 4826 - 4, NGC 5055 - 2, NGC 5194 - 5, NGC 6946 - 6, NGC 7331 - 3 Jy beam^{-1} km sec^{-1}. (right-hand column) Total intensity maps of sample galaxies. For each galaxy the vertical bar in the lower left corner shows the angular size of one kpc at the assumed distance to the galaxy. The synthesized beam is shown next to the kpc bar. For all the galaxies the contours are spaced at logarithmic intervals. Each contour is at a surface brightness of 1.585 times higher (one-half magnitude) than the previous one. The starting contour levels for the galaxies are the same as in the left-hand column.

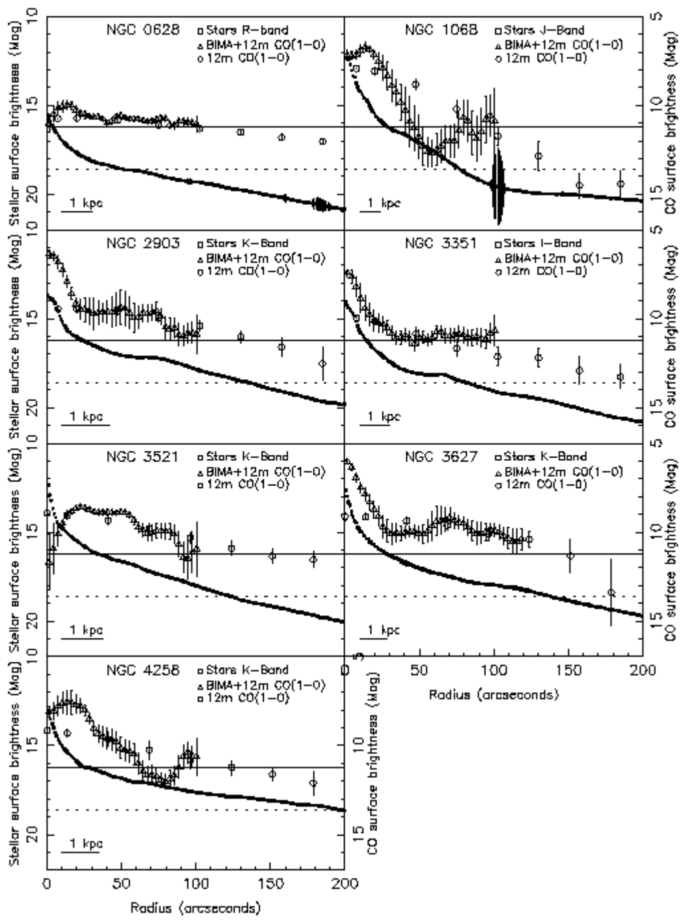

Fig. 2.— Radial profiles of the CO and stellar emission. The CO surface brightness (triangles for BIMA+12m, circles for 12m only) is in magnitudes of Jy km s^{-1} arcsec^{-2} with the zero point in magnitudes defined to be at 1000 Jy km s^{-1} arcsec^{-2}. The stellar surface brightness (squares) is in K-band magnitudes arcsec^{-2}. All points show one sigma error bars. The solid horizontal line is the noise-dependent flux level of the BIMA+12m maps that is consistent with a zero flux. Similarly, the dotted horizontal line is consistent with a zero flux level in the single dish only maps. The horizontal bar in the lower left corner shows the angular size of 1 kpc at the assumed distance to the galaxy.

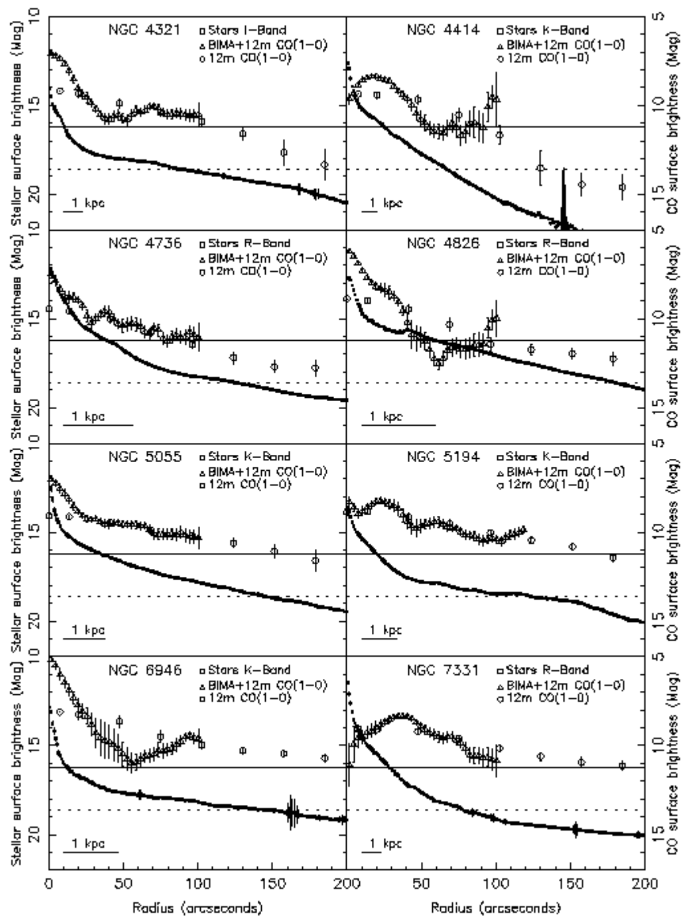
NGC 4321
Stars I–Band
BIMA+12m CO(1–0)
12m CO(1–0)
NGC 4414
Stars K–Band
NGC 4736
Stars R–Band
NGC 4826
NGC 5055
NGC 5194
NGC 6946
NGC 7331
1 kpc
Stellar surface brightness (Mag)
CO surface brightness (Mag)
Radius (arcseconds)

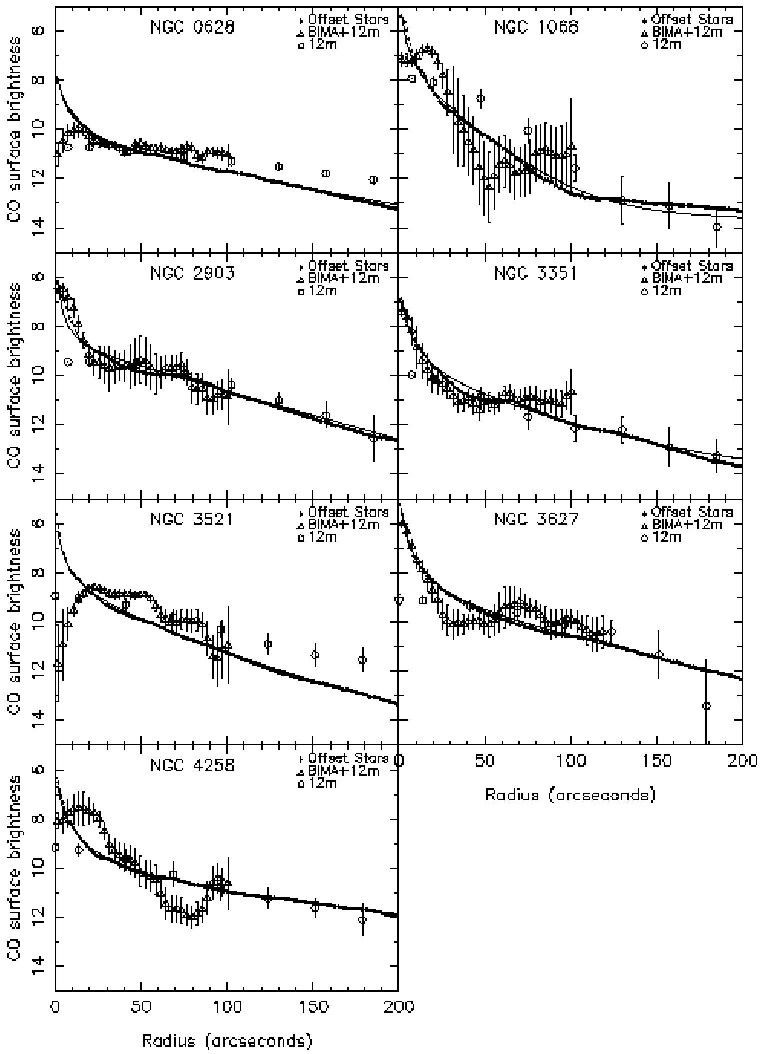

Fig. 3.— CO and offset stellar profiles. Similar to Figure 2 except that here the stellar profile has been offset to the average value of the offset between the CO+12m and the stellar profile. The asterisks are the surface brightness values of the stellar profile after offsetting. The solid line is the offset model profile. The triangles are the surface photometry of the CO+12m maps, and the circles are the surface photometry values from the 12m-only CO maps.

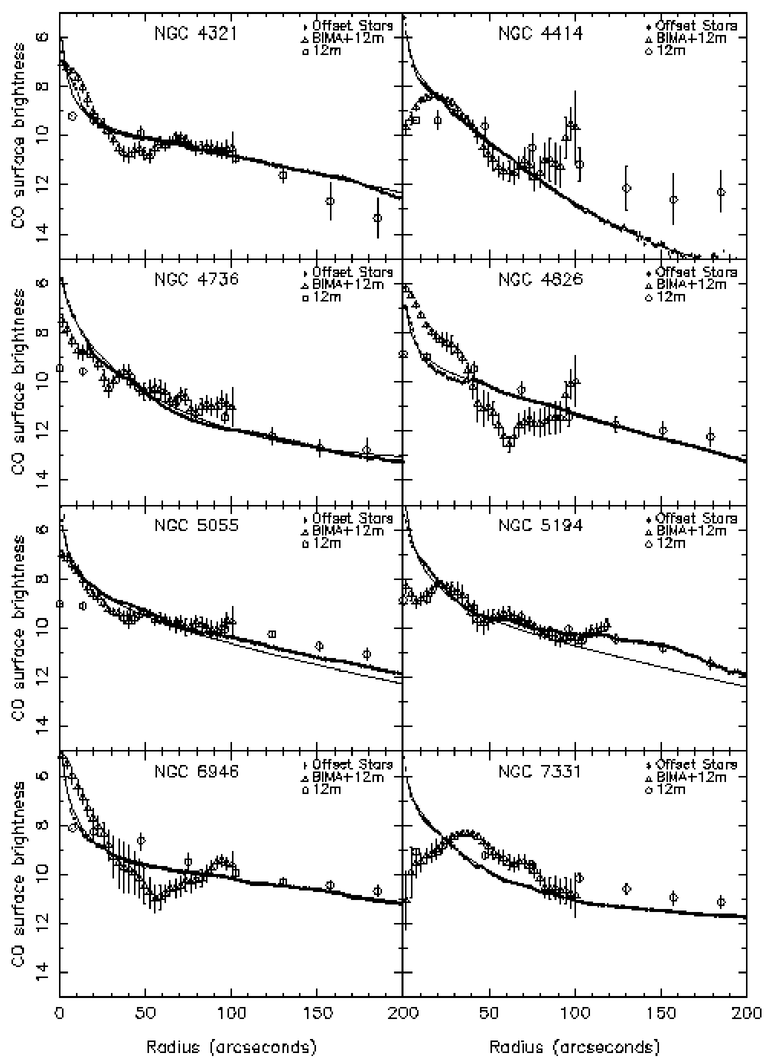
NGC 4321
NGC 4414
NGC 4736
NGC 4826
NGC 5055
NGC 5194
NGC 6946
NGC 7331
Offset Stars
BIMA+12m
12m
CO surface brightness
Radius (arcseconds)

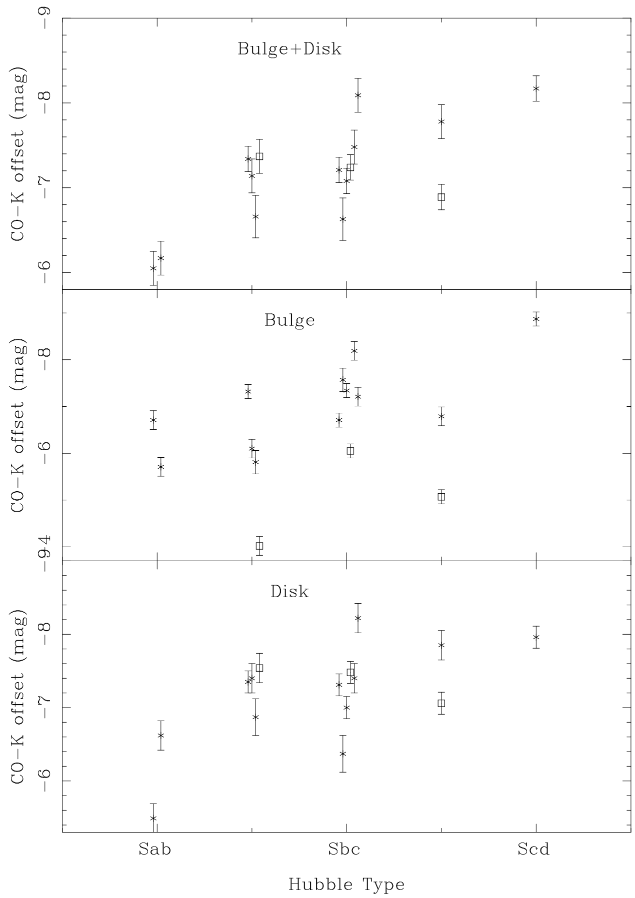

Fig. 4.— (Upper panel) CO-K offsets of the inner 200 arcsec. The total CO flux is obtained from the single dish map. The stellar observations that were not done in K-band were corrected to K-band magnitudes using published aperture photometry values. The error bars are the quadrature sum of the uncertainties in the K band magnitudes and those of the CO amplitude calibration and are dominated by the uncertainties in the CO. The three galaxies plotted as boxes are NGC 4414, NGC 3521, and NGC 7331, the three with strong central depressions in their surface brightness profiles. (Middle panel) CO-K offsets of bulge region. This is the offset of the light inside a one kpc radius. The bulge CO flux is obtained from the BIMA+12m map. (Bottom panel) CO-K offset of disk region (r $>$ 1 kpc). This is the offset of the light outside of a one kpc radius. The disk CO flux is obtained by subtracting the bulge flux obtained from the BIMA+12m map from the single dish flux inside of 200″.

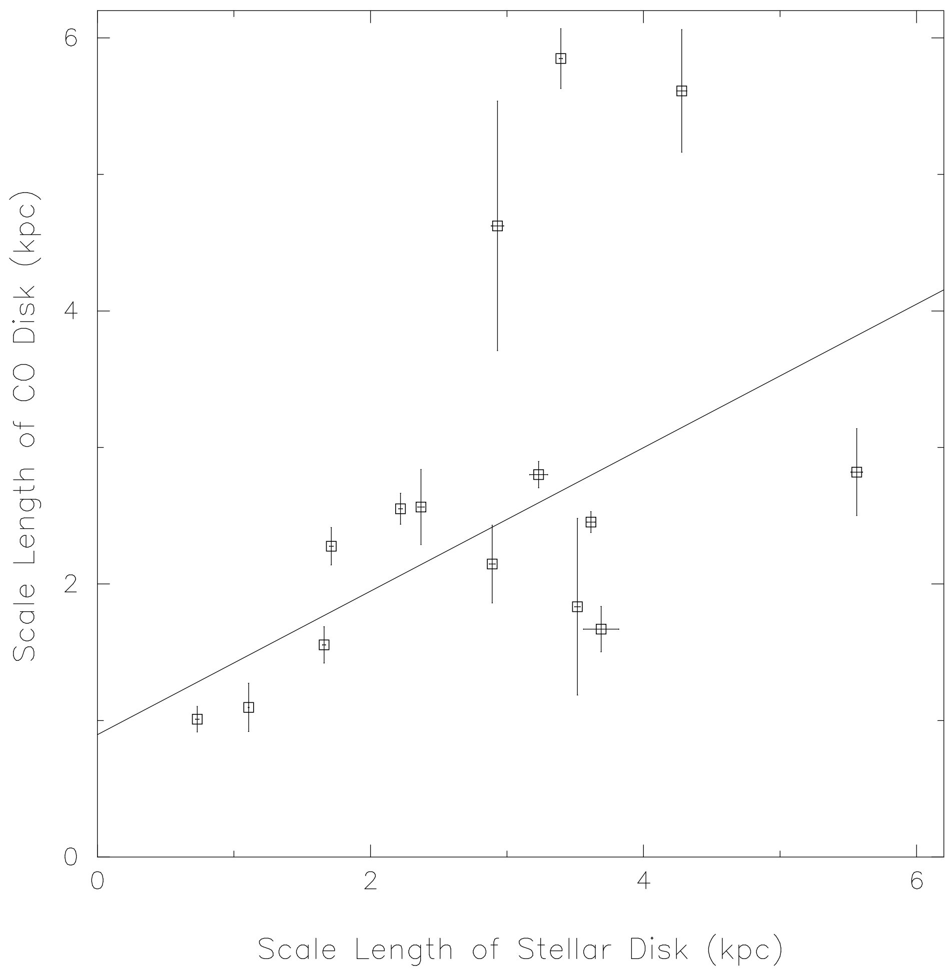

Fig. 5.— Scale lengths of CO and stellar disks. The error bars are the formal one sigma uncertainties in the fitted scale lengths. The CO scale lengths are derived from the fully sampled single dish maps. The solid line represents a linear least-squares fit.

Table 1: BIMA SONG Sample

NGC 0628	NGC 0925	NGC 1068	IC 342	NGC 2403	NGC 2841	NGC 2903
NGC 2976	NGC 3031	NGC 3184	NGC 3344	NGC 3351	NGC 3368	NGC 3521
NGC 3627	NGC 3726	NGC 3938	NGC 3953	NGC 3992	NGC 4051	NGC 4258
NGC 4303	NGC 4321	NGC 4414	NGC 4450	NGC 4490	NGC 4535	NGC 4548
NGC 4559	NGC 4569	NGC 4579	NGC 4699	NGC 4725	NGC 4736	NGC 4826
NGC 5005	NGC 5033	NGC 5055	NGC 5194	NGC 5248	NGC 5247	NGC 5457
NGC 6946	NGC 7331					

Table 2. Paper I Subsample

Galaxy	RA (J2000) $h\ m\ s$	Dec (J2000) $^\circ\ '\ ''$	$V_{\rm LSR}$ km s^{-1}	i $^\circ$	PA $^\circ$	Type	d Mpc	Distance Reference	CO beam size $''$
NGC 0628	01:36:41.70	+15:46:59.4	657	24	25	SA(s)c	7.3	1	7.1×5.2
NGC 1068	02:42:40.74	−00:00:47.7	1136	33	13	(R)SA(rs)b, Sy2	14.4	1	8.9×5.6
NGC 2903	09:32:10.05	+21:30:02.0	556	61	17	SAB(rs)bc, HII	6.3	1	6.8×5.5
NGC 3351	10:43:57.98	+11:42:14.4	778	40	13	SB(r)b, HII	10.1	2	7.3×5.1
NGC 3521	11:05:49.26	−00:02:02.3	805	58	164	SAB(rs)bc, LINER	7.2	1	8.7×5.6
NGC 3627	11:20:15.07	+12:59:21.7	727	63	176	SAB(s)b, Sy	11.1	3	6.6×5.5
NGC 4258	12:18:57.52	+47:18:14.2	448	65	176	SAB(s)bc, Sy1	8.1	4	6.0×5.3
NGC 4321	12:22:54.84	+15:49:20.0	1571	30	154	SAB(s)bc, HII	16.1	5	7.2×4.9
NGC 4414	12:26:27.19	+31:13:24.0	716	55	159	SA(rs)c?	19.1	6	6.3×5.0
NGC 4736	12:50:53.06	+41:07:13.6	308	35	100	(R)SA(r)ab,LINER	4.3	1	6.9×5.0
NGC 4826	12:56:44.24	+21:41:05.1	408	54	111	(R)SA(rs)ab, Sy	4.1	1	7.4×5.1
NGC 5055	13:15:49.25	+42:01:49.3	504	56	81	SA(rs)bc,HII/LINER	7.2	1	5.8×5.4
NGC 5194	13:29:52.35	+47:11:53.8	463	15	0	SA(s)bc-pec, Sy2.5	8.4	1	5.8×5.1
NGC 6946	20:34:52.33	+60:09:14.2	48	54	65	SAB(rs)cd, HII	5.5	1	5.9×4.9
NGC 7331	22:37:04.09	+34:24:56.3	821	62	172	SA(s)b, LINER	15.1	7	6.1×5.0

References. — (1) Tully (1988); (2) Graham et al. (1997); (3) Saha et al. (1999); (4) Maoz et al. (1999); (5) Ferrarese et al. (1996); (6) Turner et al. (1998); (7) Hughes (1998);

Table 3. Optical/Infrared Data

Galaxy	Band	image reference	X-K color	photometry reference
NGC 0628	R	Ferguson et al. (1998)	2.4	Aaronson (1977)
NGC 1068	J	Regan (2000)	1.16	Aaronson (1977)
NGC 2903	K'	Regan & Elmegreen (1997)	–	
NGC 3351	I	SONG complementary	1.65	Tifft (1961); Glass (1976); Aaronson (1977)
NGC 3521	K'	Thornley (1996)	–	
NGC 3627	K'	Regan & Elmegreen (1997)	–	
NGC 4258	R	SONG complementary	2.35	Aaronson (1977)
NGC 4321	I	SONG complementary	1.97	Boroson, Strom & Strom (1983); Aaronson (1977)
NGC 4414	K'	Thornley (1996)	–	
NGC 4736	R	SONG complementary	2.17	Johnson (1966)
NGC 4826	R	SONG complementary	–	Aaronson (1977)
NGC 5055	K'	Thornley (1996)	–	
NGC 5194	K	Gruendl (1996)	–	Aaronson (1977); Ellis, Gondhalekar & Efstathiou (1982)
NGC 6946	K	Regan & Vogel (1994)	–	
NGC 7331	R	A. Ferguson, priv. comm.	–	Aaronson (1977)

Table 4. Stellar and CO Magnitudes

Galaxy	Total			Bulge			Disk		
	CO	K	CO-K	CO	K	CO-K	CO	K	CO-K
NGC 0628	−1.00	6.78	−7.78	2.52	9.31	−6.79	−0.96	6.89	−7.85
NGC 1068	−1.45	5.69	−7.14	0.86	6.96	−6.10	−1.32	6.09	−7.40
NGC 2903	−1.07	6.01	−7.08	0.37	7.71	−7.34	−0.73	6.26	−7.00
NGC 3351	−0.13	6.53	−6.66	2.09	7.91	−5.81	0.02	6.89	−6.87
NGC 3521	−1.41	5.82	−7.24	1.16	7.21	−6.05	−1.30	6.18	−7.48
NGC 3627	−1.31	6.03	−7.34	0.73	8.06	−7.32	−1.13	6.22	−7.35
NGC 4258	−0.75	5.89	−6.63	0.47	8.04	−7.57	−0.32	6.05	−6.37
NGC 4321	−1.16	6.32	−7.48	0.97	9.16	−8.19	−1.00	6.40	−7.40
NGC 4414	−0.06	6.83	−6.89	3.67	8.74	−5.07	−0.03	7.03	−7.06
NGC 4736	−0.86	5.31	−6.17	0.16	5.87	−5.71	−0.32	6.30	−6.62
NGC 4826	−1.01	5.04	−6.05	−0.45	6.26	−6.71	−0.03	5.46	−5.49
NGC 5055	−1.52	5.69	−7.21	0.65	7.36	−6.71	−1.36	5.95	−7.31
NGC 5194	−2.37	5.72	−8.09	0.34	7.55	−7.21	−2.27	5.95	−8.22
NGC 6946	−2.13	6.05	−8.17	−0.88	7.99	−8.87	−1.71	6.25	−7.96
NGC 7331	−1.51	5.86	−7.37	3.93	7.94	−4.02	−1.51	6.03	−7.54

Table 5. Stellar and CO profile parameters

Galaxy	Stellar scale length (kpc)	CO scale length (kpc)	Central excess?
NGC 0628	3.4±0.01	5.8±0.2	no
NGC 1068	3.7±0.1	1.7±0.2	no
NGC 2903	1.7±0.01	1.6±0.1	yes
NGC 3351	2.4±0.02	2.6±0.3	yes
NGC 3521	1.7±0.01	2.3±0.1	no
NGC 3627	3.5±0.02	1.8±0.6	yes
NGC 4258	3.6±0.03	2.5±0.08	no
NGC 4321	5.6±0.04	2.8±0.3	yes
NGC 4414	2.9±0.05	4.6±0.91	no
NGC 4736	0.7±0.01	1.0±0.1	yes
NGC 4826	1.1±0.0030	1.1±0.2	yes
NGC 5055	2.2±0.01	2.6±0.1	yes
NGC 5194	3.2±0.07	2.8±0.1	no
NGC 6946	2.9±0.02	2.1±0.3	yes
NGC 7331	4.3±0.04	5.6±0.4	no